Geochimica et Cosmochimica Acta 357 (2023) 1–12

Contents lists available at ScienceDirect

Geochimica et Cosmochimica Acta

journal homepage: www.elsevier.com/locate/gca

Refined views of ancient ocean chemistry: Tracking trace element incorporation in pyrite framboids using atom probe tomography

Nicole Mae M. Atienza [a], Daniel D. Gregory [a,*], Sandra D. Taylor [b], Megan Swing [a], Daniel E. Perea [b], Jeremy D. Owens [c], Timothy W. Lyons [d]

[a] Department of Earth Sciences, University of Toronto, ON, Canada
[b] Environmental Molecular Sciences Laboratory, Pacific Northwest National Laboratory, Richland, WA, USA
[c] Florida State University, National High Magnetic Field Laboratory, Tallahassee, FL, USA
[d] Department of Earth and Planetary Sciences, University of California, Riverside, CA, USA

ARTICLE INFO

Associate editor: Brian Kendall

Keywords:
Atom probe tomography
Pyrite
Euxinic
Trace elements
LA-ICPMS

ABSTRACT

The trace element chemistry of pyrite can be used to determine the origin, timing, and conditions of formation of ore deposits; as a vectoring tool for mineral exploration; and to determine the evolution of the Earth's oceanic and atmospheric chemistry. However, little is known about whether trace elements are held with the pyrite structure or within nano-inclusions of other phases. This distinction is important for two primary reasons. First, trace element incorporation into the pyrite structure can affect the partitioning of other trace elements. Second, if trace elements are held within nano-inclusions, the partition coefficient of the mineral phases that make up the nano-inclusion, rather than pyrite, are the critical consideration in related interpretations. Previous studies addressing this topic have used laser ablation inductively coupled plasma mass spectrometry; however, the resulting data do not provide sufficient spatial resolution to delineate trace element distributions unless the inclusions are large. Further, they use these flat element profiles in time resolved laser ablation output graphs to argue that pyrite trace element content provides a direct relationship between trace element content of seawater and pyrite trace element content. To improve resolution, we have used atom probe tomography to characterize trace element distributions in pyrite framboids from the Cariaco Basin and Demerara Rise in three-dimensions at sub-nanometer resolution. Manganese was found to be concentrated in the pyrite nanocrystal part of the original framboid structure. In contrast, Ni was mostly found along the grain boundary, though it still appeared to be contained within the pyrite structure. Copper was concentrated in later pyrite overgrowths, and As varied in its location. These observations suggest that some important trace elements are incorporated into pyrite during early diagenesis, even in euxinic settings dominated by water-column pyrite formation. Statistical analysis was used to determine whether trace elements were incorporated in the lattice or within nanoscale inclusions (referred to here are nano-inclusions). We found that As, Ni, Cu, and Mn were commonly held within the pyrite structure, but As, Ni, and Cu can also be held as nano-inclusions or within grain interfaces. Incorporation of As is known to enhance the incorporation of other trace elements and in this case appears to correlated to elevated Ni and Cu concentrations in the Cariaco Basin samples. Understanding these relationships strongly impacts our ability to utilize pyrite trace metal concentrations to analyze and quantify early ocean chemistry and its evolution through time.

1. Introduction

Pyrite (FeS_2) is the most abundant sulfide mineral in the Earth's crust and can be found in almost all environments, including igneous, metamorphic, and sedimentary rocks (Rickard, 2012). It also shows variable size (from cm to nm scale) and textural (e.g., euhedral/anhedral, nodule, framboidal) variations. Framboids are spherical to subspherical clusters of numerous microcrystals of pyrite and are found predominantly in sedimentary environments (Wang and Morse, 1996; Wilkin and Barnes, 1997; Rickard, 2021). The applications of trace element compositions in pyrite are wide ranging and include: (1) the origins, timings, and conditions of ore deposit formation (Huston et al., 1995; Meffre et al., 2008;

* Corresponding author.
E-mail addresses: nicole.atienza@utoronto.ca (N.M.M. Atienza), daniel.gregory@utoronto.ca (D.D. Gregory).

https://doi.org/10.1016/j.gca.2023.07.013
Received 20 November 2022; Accepted 14 July 2023
Available online 17 July 2023

Large et al., 2009); (2) as a vectoring tool for mineral exploration (e.g., Cassidy et al., 1998; Gregory et al., 2016; Belousov et al., 2016; Fougerouse et al., 2019); and (3) determinations of the evolution of ocean and atmosphere chemistry (Large et al., 2014; Gregory et al., 2017; Fougerouse et al., 2019). Pyrite is also an important sink for heavy metals and metalloids (e.g., As) in contaminated rivers and estuaries (Lowers et al., 2007). Therefore, an understanding of the factors that control the enrichment of trace metals into pyrite is essential (Gregory et al., 2014; Fougerouse et al., 2019).

Trace elements can be incorporated into pyrite in two ways: substitution into the pyrite structure or as inclusions of different mineral or amorphous phases. When a trace element is incorporated into the pyrite structure, it substitutes for either Fe or S (Reich and Becker, 2006; Deditius et al., 2008; Qian et al., 2013; Gregory et al., 2015), whereas trace elements incorporated as nano-inclusions exist as distinct minerals or amorphous masses within the pyrite. Previous studies used laser ablation-induced coupled plasma-mass spectrometry (LA-ICP-MS) to determine how trace elements are incorporated into pyrite (Gregory et al., 2015). Gregory et al. (2015) reasoned that Ni, Co, and As are incorporated in the pyrite structure because of their uniform distributions in time-resolved laser ablation output graphs. However, analyses based on two dimensional (2D) graphs and the relatively large spot size of LA-ICP-MS (10–100 μm) are not sufficient to confidently resolve trace elements substituted into the pyrite lattice versus those in evenly distributed in nanoscale inclusions. In contrast, atom probe tomography (APT) is a powerful technique that reconstructs the elemental and isotopic composition of materials in three-dimensions (3D) with sub-nanometer resolution and part-per-million sensitivity (Gault et al., 2021; Miller and Forbes, 2009; Miller and Forbes, 2014; Reddy, et al., 2020). Previous APT studies have focused on the association of Au (Fougerouse et al., 2016; Wu et al., 2019; Fougerouse et al., 2019), As (Wu et al., 2019), and Cu (Wu et al., 2019) within pyrite. Building on these studies, we evaluate spatial locations for all detectable trace elements in pyrite framboids (formed in sedimentary environments) using APT and complementary statistical analyses to determine how each trace element is associated within pyrite.

Pyrite trace element content has been argued to reflect trace element composition of past oceans (Large et al., 2014). However, more recent studies have observed that pyrite trace element concentration varies with depth of sediments until reaching a relatively steady composition (Gregory et al., 2022b). Thus, the relationship between water column trace content and pyrite trace element concentration can be complicated, reflecting both water column and pore water composition, including modifications via release of trace elements from organic matter and/or Fe (hydr)oxides during diagenesis (Tribovillard et al., 2006; Gregory et al., 2015).

Arsenic is particularly well studied for its incorporation into pyrite due to its ability to enhance uptake of other elements into pyrite, its close association with Au, and its environmental implications (Deditius et al., 2008; Gregory et al., 2015). Arsenic can be incorporated into pyrite through substitution with either S^{2-} or Fe^{2+} (Reich and Becker, 2006; Deditius et al., 2008; Qian et al., 2013; Gregory et al., 2015) or as unstructured As-Fe-S nano-inclusions trapped in pyrite (Deditius et al., 2008). The substitution of As for S can increase the uptake of elements with ionic radii and charges similar to those of Fe^{2+}, such as Co^{2+}, Ni^{2+}, and Cu^{2+}, while the substitution of As^{3+} for Fe^{2+} will enhance the uptake of large cations such as Au^{1+}, Ag^{1+}, and Pb^{2+} (Michel et al., 1994; Deditius et al., 2008; Gregory et al., 2015). This relationship reflects the charge imbalance when As^{3+} substitutes for Fe^{2+}, which distorts the pyrite lattice or creates vacancies that allow incorporation of large cations (Cook and Chryssoulis, 1990; Fleet and Mumin, 1997; Deditius et al., 2008). As a result, the As concentration in pyrite may significantly influence the concentration of other incorporated elements (Reich et al., 2005; Deditius et al., 2008).

Graphs of time-resolved laser ablation output charts (Gregory et al., 2015) provide indirect insight for how trace elements incorporate into pyrite. They interpreted peaks in the graphs to indicate when the trace element was incorporated into microscale inclusions, while relatively flat plots were interpreted to indicate lattice incorporation. In addition to micro-inclusions these increases in trace element content could be due to trace element heterogeneity within the pyrite framboid, like those shown at grain boundaries (Gregory et al., 2022a). However, these indirect observations are only suggestions of how trace elements associate with the mineral phase and how compositions may evolve temporally (e.g., relative to different generations of pyrite).

Atom probe tomography provides 3D representations of where atoms are situated at nanometer scales in a needle-shaped sample of the target mineral. This resolution is achieved by placing the sample in an electric field such that the specimen is attracted by a local electrode. A laser is then applied to the sample, with the result that atoms are accelerated toward a position-sensitive time of flight mass spectrometer detector. Depending on when and where the atoms are detected, the placement of the atoms within the original sample tip can be reconstructed.

As a 3D chemical imaging technique, with high-resolution and chemical sensitivity, APT is uniquely suited to probe directly the modes and mechanisms of trace element incorporation spatially and temporally across mineral phases (Reddy et al., 2020, Taylor et al., 2019). In particular, recent studies capturing the spatial and temporal distribution of elements within pyrite reveals nanoscale chemical heterogeneities that correlate to unique crystal growth mechanisms and environmental controls. For instance, characterization of the distribution of Au in arsenopyrite in 3D revealed heterogeneities of Au and As in the mineral that were not observable with traditional LA-ICPMS analyses (Fougerouse et al. 2016), providing insight as to how arsenopyrite can host large quantities of gold relevant to many economically significant deposits. A similar study by Fougerouse et al. (2019) analyzed pyrite from the Witwatersrand Basin, revealing the heterogeneous distribution of trace elements and Pb isotopes in pyrite that were not observed in LA-ICPMS studies (Large et al., 2013). Observations of As-rich nanoscale fluid inclusions point to mechanisms of element segregation in a brittle-dominated deformation regime (Dubosq et al., 2020; 2021). Further, insight into trace element incorporation mechanisms has been gained through studies of trace element (Au, As, Cu) zoning within pyrite in an Au-rich arsenian pyrite from an orogenic gold deposit from Daqiao, China (Wu et al. 2019).

In this paper, we seek to understand how trace elements are incorporated into framboidal pyrite from euxinic sedimentary environments using APT with the goal of assessing how trace elements are contained within pyrite framboids as well as whether certain elements could enhance the uptake of others. We focus on relationships between pyrite elemental composition and modern environmental controls, which can be both local and global. We compare these analyses to depth-resolved and *in situ* analyses by LA-ICP-MS, demonstrating that some trace element abundances increase with sediment depth even in euxinic settings where pyrite is thought to form largely in the water column (Gregory et al., 2022b). This observation has implications for how pyrite trace element content can inform our understanding of past ocean chemistry, as well as trace element availability during different stages of diagenesis with implications for biogeochemical cycles and microbial ecology in the subsurface.

2. Methods

2.1. Samples

The pyrite framboids analyzed in this study are from the Cretaceous Demerara Rise in the Atlantic Ocean off the coast of Suriname and the modern Cariaco Basin off the coast of Venezuela. These locations were chosen because both record euxinic deposition with open connections to the ocean and geochemistry that is relatively well understood based on previous studies. Additionally, the trace element content in pyrite framboids from the Cariaco Basin were previously examined by Large

et al. (2014) by LA-ICP-MS, providing independent measurements for comparison. Framboids from the Demerara Rise were sampled at Ocean Drilling Project (ODP) site 1258 (9°26.000′N, 54°43.999′W) (Mosher et al., 2007). This site was chosen to be representative of water column-formed pyrite formed under locally euxinic conditions in a larger oxygenated ocean (Raven et al., 2019), much like the Cariaco Basin – the second largest anoxic basin in the modern world (Lyons et al., 2003). The samples from the Cariaco Basin are from ODP core site 1002 (10°42.366′N, 65°10.179′W) collected in 1996. Framboids were collected at a depth of 365 cm within the zone of euxinic deposition (Leckie et al., 2000; Lyons et al., 2003). Sediments from this depth were deposited approximately 9400 years before present (Hughen et al., 1998; Hughen et al., 1996a; Hughen et al., 1996b). This site was chosen to represent relatively recently formed water-column pyrite from a euxinic basin with open access to a mostly oxygenated regional and global ocean. Further, the sediments from this site have been used in several past studies emphasizing commonly employed geochemical proxies, including redox sensitive trace elements (Piper and Dean, 2002; Lyons et al., 2003), S isotopes (Lyons et al., 2003), N isotopes (Thunell et al., 2004), Cr isotopes (Gueguen et al., 2016), and Mo and U isotopes (Brüske et al., 2020), among others. This approach results in a large amount of complementary data for the pyrite framboid analyses. Further, by looking at relatively recent and Cretaceous samples we also assess whether extended burial can significantly alter how trace elements are held in pyrite—for example, whether trace elements reorder themselves and develop into nano-inclusions long after deposition.

2.2. Sample preparation

Framboids of interest from the Cariaco Basin and Demerara Rise were identified with reflected light microscopy at the University of Toronto. Samples were chosen to be representative of the pyrite framboids in the sample in terms of approximate size, shape, order of the microcrystals, and size of microcrystals. Representative SEM images of framboids from the Cariaco Basin and Demerara Rise are given in Fig. 1. The framboids were then prepared for analysis using conventional focused ion beam (FIB) milling techniques to produce needle-shaped APT specimens (Thompson et al., 2007). Specimens were collected across the framboid to ensure both the microcrystals that make up the framboid and the later pyrite that cements the framboids was sampled. A dual-beam FIB-SEM was used (Thermo Fisher Scientific Helios Nanolab 600i) at the Environmental Molecular Sciences Laboratory (EMSL) at Pacific National Northwest Laboratory (PNNL; Richland, WA, USA).

The approach is summarized here, see Appendix 1 in supplementary materials for details. First, a protective Pt capping layer (~100 nm) was deposited on a rectangular section of the identified framboid surface (e.g., ~4 × ~15 μm) via the electron beam, followed by a thicker coating with the ion beam (~1 μm), protecting the framboids from damage and Ga implantation during ion milling. The goal was to capture microstructural features such as grain boundaries between the microcrystals that make up the framboid and to probe trace element incorporation and distributions in the framboids. The framboid substructure was viewed in cross-section by trenching normal to the section, on both sides. The section was milled into a wedge-shaped lamella and extracted with an Omniprobe micromanipulator (Larson et al., 2013a). The liftout was in turn sectioned further and mounted onto Si microposts. Each post was sharpened into needle-shaped tips through annular milling, where the outer-edges of the section were progressively milled away (Larson et al., 2013b). An accelerating voltage of 30 kV was applied, while progressively decreasing the beam current. Nearing the final tip diameter (e.g., <100 nm), a final 2 kV accelerating voltage was applied to remove surface beam damage. This preparation scheme was used to generate six APT tips (referred to as specimens hereafter) for the Cariaco Basin and five for the Demerara Rise.

2.3. Atom probe analysis

APT analysis was performed at the EMSL user facility located at PNNL using a CAMECA Local Electrode Atom Probe (LEAP) 4000X-HR in laser-assisted mode. Specimens were run using a set-point temperature of 40 K (stage temperature 45 K), a laser pulse repetition rate of 100–250 kHz, and a detection rate of 0.002 ions per pulse (maintained by varying the applied specimen voltage). The laser wavelength was 355 nm^{-1}, and laser energy per pulse ranged from 35 to 65 pJ.

Four of the six specimens were successfully analyzed for the Cariaco Basin (specimens #13379, 13380, 13384, and 13490; the other two fractured before sufficient data could be collected). All Demerara Rise specimens were successfully measured (specimens #13367, 13369, 13370, 13676, 13679) and were viable for data analysis. On average, data successfully acquired on a single specimen (which did not fracture) took ~5 hr and yielded > 1 million ion counts. See Table S-1 in the supplementary information for data on each specimen.

2.4. Data reconstruction

Three-D chemical reconstruction of the specimens was done using the Integrated Visualization and Analysis Software (IVAS, v. 3.8.2) developed by CAMECA. The reconstruction was achieved by voltage mode where, importantly, the evaporation field was adjusted to 19.1 V/nm for pyrite based on recently established voltage reconstruction parameters by Fougerouse et al., (2019). The average atomic density for pyrite was also set to 0.013 nm^3 $atoms^{-1}$.

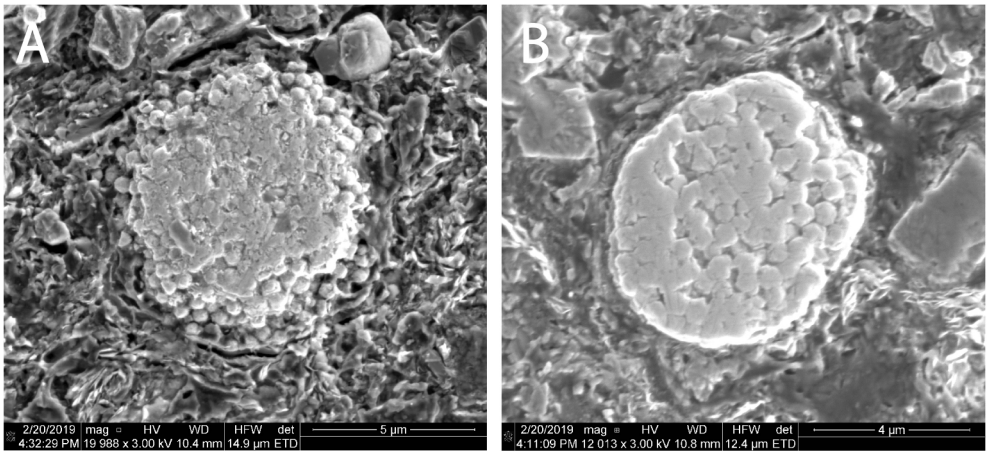

Fig. 1. SEM images of representative pyrite framboids. A) is from the Cariaco Basin and B) is from the Demerara Rise. Note that the Demerara Rise framboids tend to be more cemented than those from the Cariaco Basin.

Elemental and molecular species were initially assigned to mass peaks that had counts more than twice above the background level and pre-determined by the LEAP instrument during the sample run. The assignment of mass peak identities was refined using ratios of the isotopes of elements of interest and previous compositional knowledge of the samples from LA-ICP-MS data. The specimen chemistry was reconstructed by assigning ionic species to each mass-to-charge state peak in the generated spectra to best reproduce the expected elemental and isotopic compositions. The mass spectrum for the Cariaco Basin sample 13379 is shown as a representative example in Fig. 2. Identification of the major Fe, S, and Fe-S species was facilitated by analysis of a pyrite standard and by referring to previous APT characterizations of this mineral (Dubosq et al., 2019; Fougerouse et al., 2019; 2021, Gopon et al., 2019; Wu et al., 2019; Taylor et al., 2022). The specific peaks used to identify the trace elements of interest (i.e., Mn, As, Cu, and Ni) are marked in bold in the figure. The assignment of the trace elements was informed by previous LA-ICP-MS analyses (Large et al., 2014). Some impurities, including alkalis and/or organic matter (e.g., Na, C), are also present but are not the focus of the current study.

Elemental compositions were based on the decomposed atomic counts, with the background noise subtracted. The error in the concentrations was determined by standard counting statistics (σ_i) (Eq. (2)):

$$\sigma = \sqrt{\frac{C_i(1-C_i)}{N}}, \tag{2}$$

where C_i is the measured concentration of the element i (atomic %), and N is the total number of atoms detected.

Trace element concentrations in atomic percent were converted to weight percent (wt %) and parts per million (ppm) (Eqs. (3) and (4)):

$$wt\% = \frac{(atwt.)(at\%)}{sum\ \ of\ \ all\ \ ions\ \ detected} * 100 \tag{3}$$

$$ppm = wt\% \times 10^4, \tag{4}$$

where *at wt.* is the atomic weight of the element, and *at %* is the atomic percent stated in the bulk composition of the specimen in IVAS.

From the reconstruction, the distribution of trace elements was visualized in 3D, and concentrations were spatially quantified using concentration profiles. Based on visual inspection, of the specimen reconstructions we emphasized concentrations within specific regions of interest (e.g., those enriched in trace elements) were analyzed. To complement visual inspections, statistical analyses and random comparator techniques were conducted based on nearest neighbor (NN) distribution analyses to quantitatively describe the extent to which trace

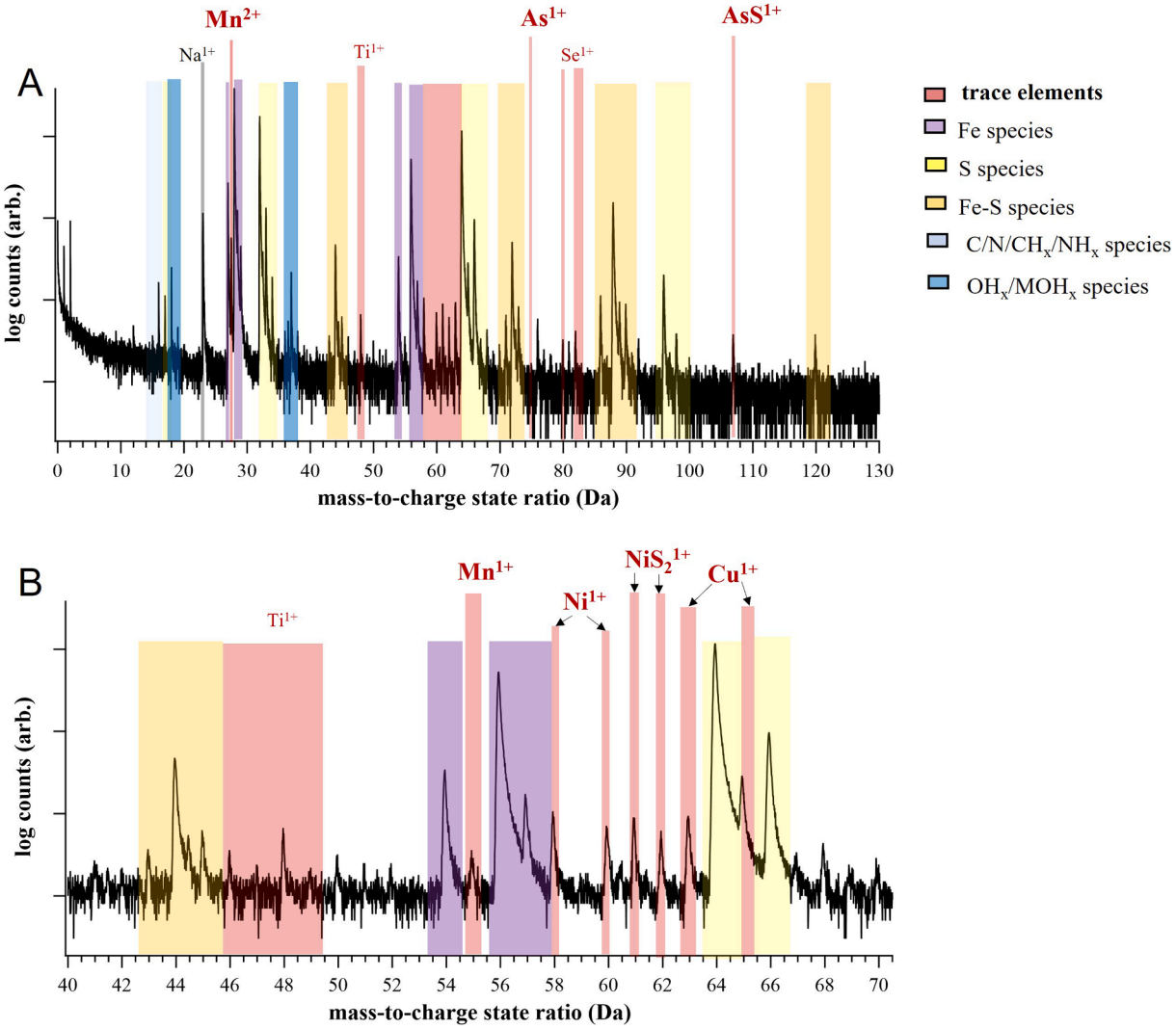

Fig. 2. Counts of mass to charge spectra used to reproduce expected elemental abundance. The specific peaks used to reconstruct the spectra are given in the figure. A) gives the counts with mass to charge ratios ranging from 0 to 130 Da. B) gives the same spectra except with the region of interest focusing on 40 to 70 Da, the area where most of the elements of interest are found.

elements may segregate or cluster (Perea et al., 2015; Stephenson et al., 2007; Taylor et al., 2018; and Taylor et al., 2022). That is, NN analysis measures the distance from one ion to another and compares these data to a simulated dataset where the ions are randomly or homogeneously distributed within a material. The deviation in the NN distributions between the experimental versus simulated datasets is quantified based on the Pearson coefficient (μ) to describe the tendency for an ion to cluster/segregate, which is determined by quantifying the deviation between the experimental and simulated datasets (Eq. (5)):

$$\mu = \sqrt{\frac{\chi^2}{N+\chi^2}}, \tag{5}$$

where N is the number of discrete blocks, and χ^2 defines the experimental deviation from randomness (Eq. (6)):

$$\chi^2 = \sum_{n=0}^{n_b} \frac{(e(n)-f(n))^2}{f(n)}. \tag{6}$$

Parameter $e(n)$ is the number of data counts at concentration n, and $f(n)$ is the randomized counts. Ultimately, if $\mu = 0$, the trace element distribution in the experimental dataset is entirely random, consistent with that expected if pyrite was homogeneously incorporated into the pyrite lattice. If $\mu = 1$, the distribution is non-random, and there is a spatial association among the atoms, consistent with that expected if the trace element is associated with nano-inclusions or segregated in microstructural features of the pyrite. As shown below, segregation also occurs to varying extents.

For NN analyses in IVAS, the sample bin width (d_{pair}) was set to 0.2 nm, and the order was set to 1 to measure the first nearest neighbor distance (when the order is set to 2, the second nearest neighbor is identified).

3. Results

3.1. Trace element compositions

The bulk composition and trace element context from both the Cariaco Basin and Demerara Rise was extracted based on mass spectral analyses (Table 1). Arsenic, Ni, Cu, and Mn, are consistently measured in most the specimens from both sites, and Co was measured in some specimens. Table 1 gives trace element content of the elements of interest in each sample from the pyrite framboids from Demerara Rise and Cariaco Basin. Total ion counts were lower than those found in other pyrite atom probe studies (Fougerouse et al., 2019; Gopon et al., 2022), which is likely because our study targeted microcrystal interfaces that are structural weak points, which led to tip breakage earlier than other studies. Further, the fact that we analyzed at temperatures 20 K lower than those of other studies (e.g. Gopon et al., 2022) may have also been a factor.

3.2. Mapping trace element distributions

The trace element distributions were visualized in 3D for the Demerara Rise and Cariaco Basin specimens to observe the spatial distributions and potential correlations among the elements of interest. Relative enrichments of trace elements are identified by increasing density of atoms as shown in the reconstruction (Figs. 3 and 4). One of the APT specimens for the Demerara Rise framboid (Fig. 3, #13676) shows a linear feature enriched in Ni and Cu. Interestingly, in specimen #13676 Ni and Cu do not correlate with As and this is the only specimen that did not have significant quantities of As occurring as AsS. Manganese is enriched near the base of the specimen. Another specimen (Fig. 3, #13370) does not exhibit regions enriched in trace elements—i.e., Ni, As, Cu, and Mn, are all evenly distributed. In specimen #13367 (Fig. 3), Cu atoms are localized at the apex of the needle shaped specimen. Nickel also appears in the apex region, although its enrichment is less clear than that of the Cu atoms. Based on visualization of the elements within the sample, there does not seem to be a correlation between Cu/Ni and Mn. Specimen #13679 does not show relative enrichments in As, Ni, or Cu; Mn is higher at the specimen base. Copper, Mn, and Ni are all evenly distributed in specimen #13369. No clear trace element enrichments can be seen in this sample.

Compared to Demerara Rise specimens, those from the Cariaco Basin showed more segregation into specific features or zones (the microstructure that may align with this distribution is discussed below). Specimen #13379 (Figs. 4 and 5) has regions with Mn alternating between high and low concentrations. Fig. 5 shows these zones, which are separated with red dashes and labeled L1 and L2 for the low concentration Mn zones and H1 and H2 for the high concentration zones. Conversely, Ni, Cu, and As are enriched within the low Mn concentration zone. Nickel, Cu, and As are present in a zone of trace element enrichment that occurs on the margin of the specimen and is subparallel to the axis of the specimen. Further, regions enriched with Cu, Ni, and As also overlap with each other.

Reconstructed maps of specimens #13380, 13384, and 13490 can also be found in Fig. 4. Similar to specimen #13379, Mn in #13380 also appears to be segregated into zones. In the low concentration zones for Mn, Cu and As tend to have higher concentrations. Nickel does not appear to correlate with other trace elements and is evenly distributed in the specimen. Manganese zoning is also present in specimen #13384; however, there is no apparent correlation between its zoning and other high trace element concentrations. Nickel and Cu, however, seem to be highly concentrated on one side of the specimen. This tip had the lowest ion count (500 K ions), and there are insufficient data to determine correlations with other trace elements. APT specimen #13490 from the Cariaco Basin is again zoned in Mn, and As, Ni, and Cu. Concentrations of these are elevated in areas where Mn concentrations are low. The high concentrations of these trace elements occur as a linear feature through the specimen approximately parallel to the tip's axis.

Overall, the Cariaco Basin specimens consistently show zones

Table 1
Trace element content of APT specimen tips.

	Mn (ppm)	Mn error (%*)	Ni (ppm)	Ni error (%*)	Co (ppm)	Co error (%*)	Cu (ppm)	Cu a error (%*)	As (ppm)	As error (%*)
Demerara Rise										
13367	970	8.5	3960	4.4			22,200	1.9		
13369	150	20	1020	7.7					110	27
13370	45	6.9	317	2.7	37	7.8	297	2.9	55	2.9
13676	110	9.2	1860	2.4	140	8.6	650	4.1	180	8.6
13679	235	3.5	30	20			140	9.7	100	12
Cariaco Basin										
13379	4280	3.1	4010	3.3			1380	5.9	720	8.8
13380	2980	6.0	3220	6.0			280	21	550	8.1
13384	4390	5.4	1800	8.7			490	17	530	18
13490	7210	2.7	760	8.5	140	20	170	19	480	12

* Error given is 2 sigma.

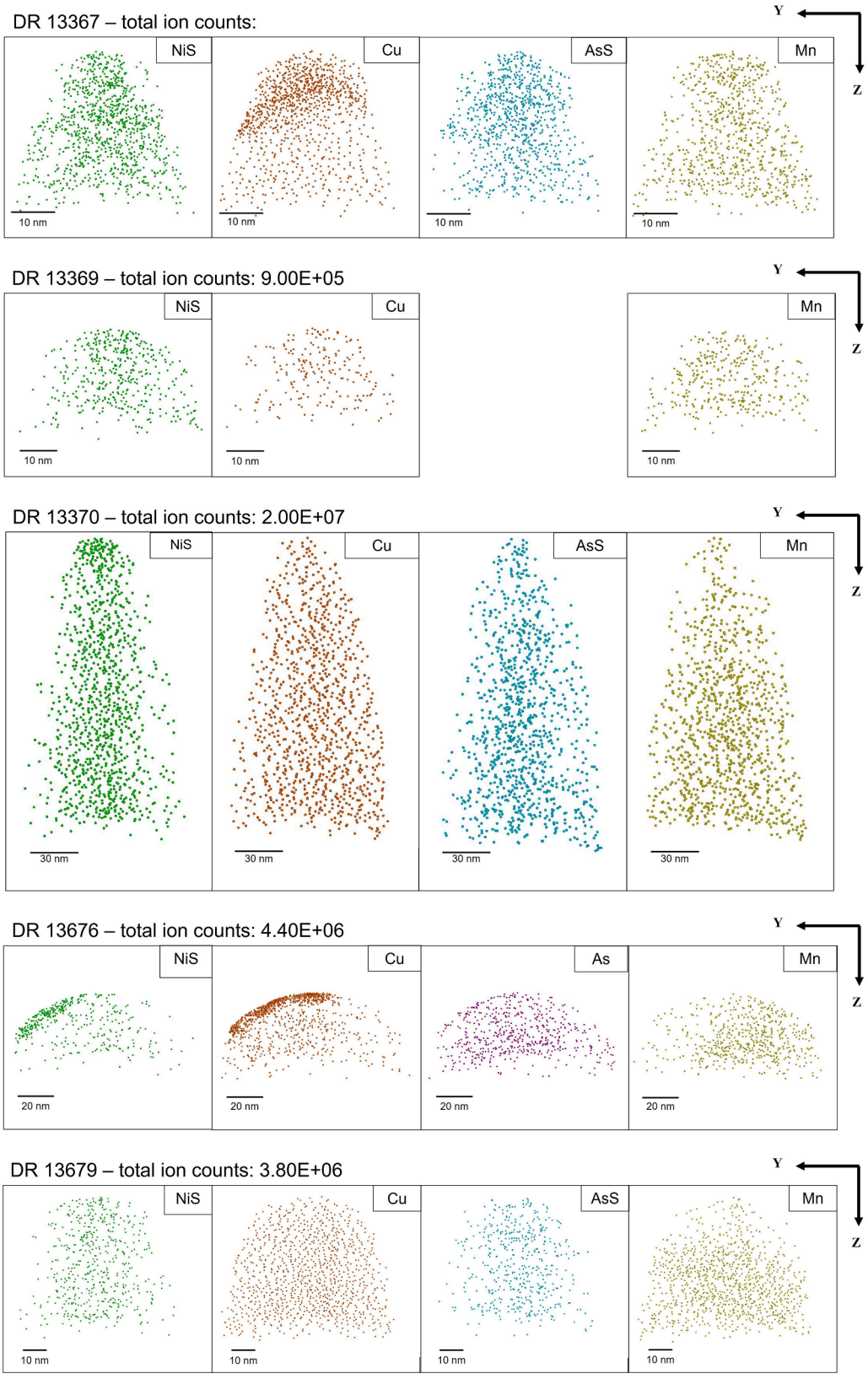

Fig. 3. 3-D trace element atom map reconstruction of Demerara Rise samples (X axis extends out of the page). The individual colored spots in the figure indicate the location of the specific atom in the sample. Generally, AsS gave the best representation of As abundance and was used except for DR13676 where AsS was in low abundance, here As was used instead. Further DR13369 had all As species below detection limits. Note the instrument can detect ~40% of the atoms in the sample.

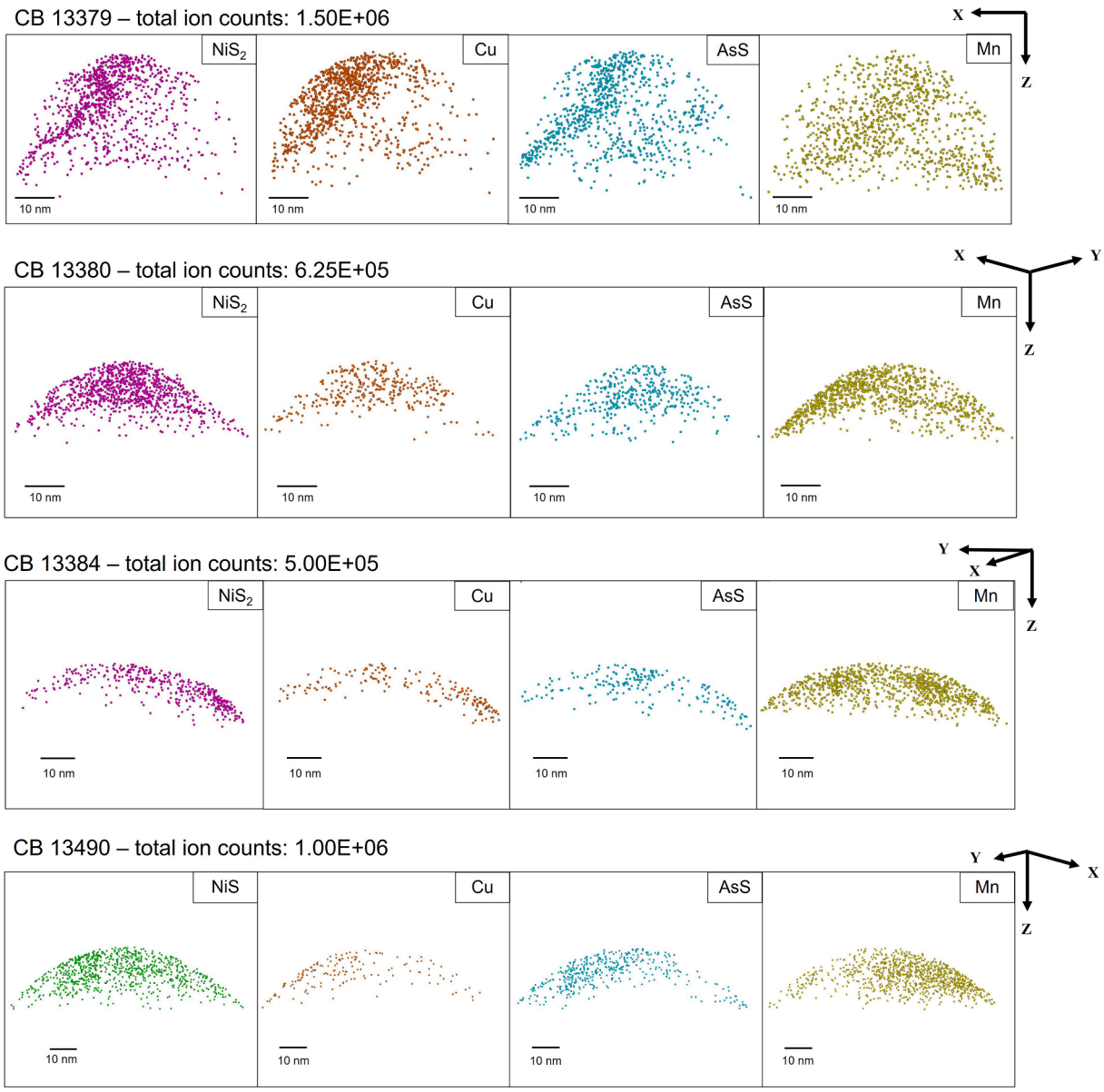

Fig. 4. 3-D trace element atom map reconstruction of Cariaco Basin samples. For CB13379 Y axis extends out of the page. The individual colored spots in the figure indicate the location of the specific atom in the sample. Generally, NiS_2 gave the best representation of Ni abundance and was used except for CB13490 where NiS was used instead. Note the instrument can detect ~40% of the atoms in the sample.

alternating between low and high Mn concentrations. High concentrations of other trace elements are also found within the low Mn concentration zones. The high concentrations of trace elements tend to occur in planar features. Trace elements in the Demerara Rise samples have fewer apparent microstructural features, showing a more uniform distribution. Demerara Rise specimens #13367 and #13676 are the only samples with clear elemental zonation. Demerara Rise specimen #13676 shows the strongest correlation among the trace element for specimens from this location.

3.3. Compositional zoning in Cariaco Basin framboids

The Cariaco Basin samples show clear trace element zoning, and further compositional analysis of these zones was conducted to determine the concentration of trace elements in each of the zones. Cariaco Basin APT specimen #13379 was chosen for this analysis as it contains the clearest Mn zoning, with two low concentration zones and two high concentration zones (Fig. 5A). This sample also contains the highest number of detectable trace elements (As, Ni, Cu, Co, and Mn). Each zone was isolated in IVAS, and the atomic bulk compositions of As, Ni, Cu, and Mn, plotted (Fig. 5B).

Nickel dominates in zone L1 (~0.9 atomic %), followed by Cu > Mn > As (Fig. 5B). Manganese is enriched in zone H1 (~0.6 atomic %), followed by Ni > As > Cu. Zone L2 is a low concentration zone for Mn, with Ni > As > Cu. Finally, Zone H2 is a high concentration zone for Mn with ~ 0.8 atomic %, followed by Ni > Cu > As.

3.4. Distribution of trace elements: A statistical analysis

NN statistical analyses were performed to explore the degree to which different atoms are spatially correlated to one another, testing visual interpretations of atomic map distributions. The resulting distribution plot for a trace element from the NN analysis shows the comparison between experimental (Cariaco basin and Demeraera Rise APT specimens) and random simulations. If the sample plots are statistically similar to those for random simulations (Fig. 6A), it is logically inferred

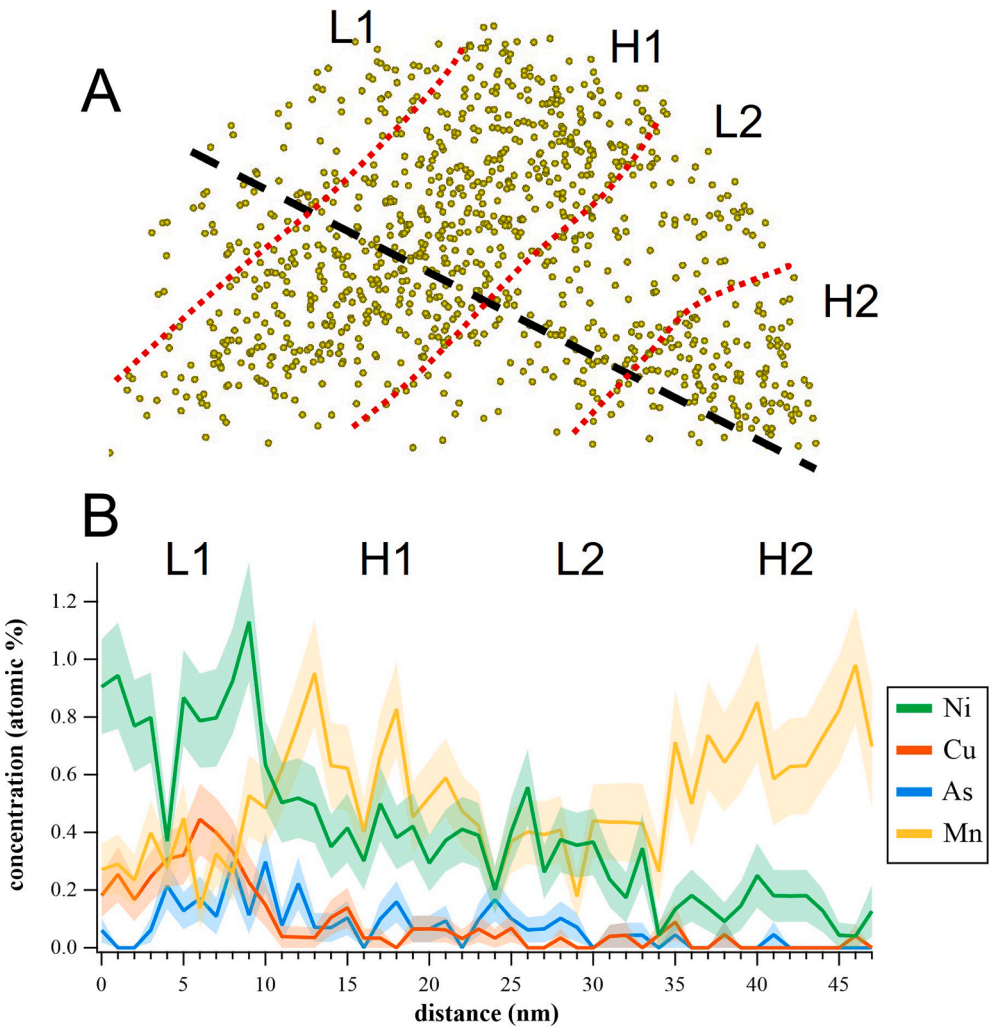

Fig. 5. A) Trace element reconstruction highlighting the zones denoted by Mn concentration in Cariaco Basin sample #13379. L1 and L2 are low concentration Mn zones as indicated by the lack of Mn atoms in these areas. H1 and H2 are high concentration Mn zones as indicated by the relatively abundant Mn atoms in these areas. B) Selected region of interest and its 1D concentration profile of trace elements showing relationships with the different elements. In this figure we can see the presumed grain interface with later, more trace element enriched pyrite on the left of the plot followed by two bands of Mn enrichment. The presence of the grain interface is interpreted based on Ni and Cu enrichment also being identified in the intermicrocrystal pyrite in the Caraico Basin and Demerara Rise using TEM (Gregory et al., 2022a).

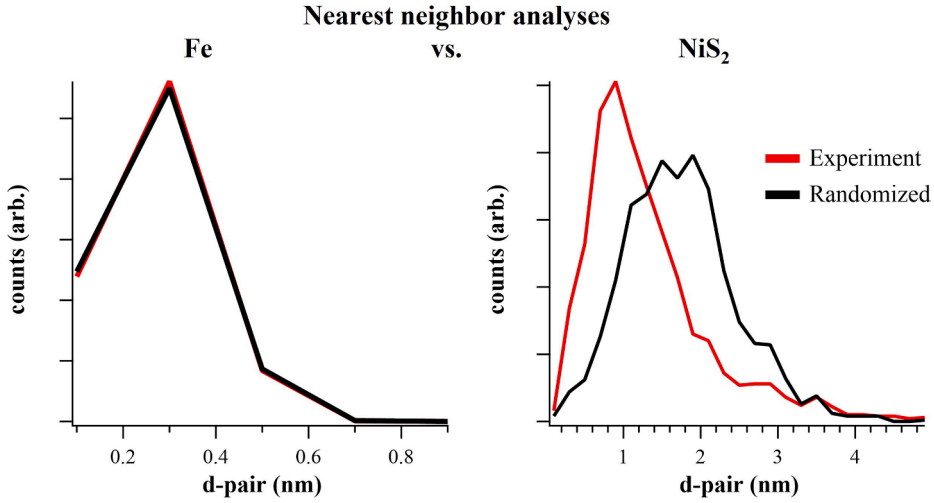

Fig. 6. Nearest neighbor distribution plot of Fe and Ni from Demerara Rise sample #13370. Random simulation is in black while the experimental data is shown in black. A) Similar plots with no deviation suggest a completely random distribution of Fe. B) Deviance between plots suggest that the distribution of Ni is non-random hence, there is spatial association between atoms.

that there is a random distribution of atoms in the samples. Statistically relevant differences reflect non-random atom distributions in the samples (Fig. 6B).

As mentioned earlier, the Pearson coefficient μ determines the relative strength of randomness in the elemental distribution. By this method, if the calculated μvalue equals 1 for a given trace element, the

distribution of atoms/ions is considered to be strongly non-random, implying a strong spatial association between the atoms. At the other extreme, if μ equals 0, the distribution of atoms/ions is completely random. In this study, we observed varying extents of segregation and described this using the following data ranges: if $\mu < 0.25$, the distribution of atoms is predominantly random; if $0.25 < \mu \leq 0.5$, the distribution is mostly random with a subset of atoms that are non-random; if $0.50 < \mu \leq 0.75$, the distribution is mostly non-random with a subset of random atoms; and if $\mu > 0.75$, the distribution of atoms in the sample is predominantly non-random. Note, these designations are approximations used to simplify the discussion.

For the Demerara Rise specimens, As, Mn, Ni, and Cu were selected for NN analysis given their presence in all the datasets (Table 2). The Pearson coefficients for all elements of Demerara Rise specimens are summarized in Table 2. In general, As and Mn are mostly random across the specimens, i.e., median μ values are 0.40 and 0.22, respectively, which is consistent with visual estimates of the atomic distributions. Nickel and Cu show some variability in their distributions, e.g., Cu ranges from mostly random to predominantly non-random (i.e., μ = 0.16–0.89). In instances where Ni and Cu segregate to microstructural features such as microcrystal interfaces, the distributions are predominantly non-random (e.g., for specimen 13676, the μ values are 0.96 and 0.89, respectively), consistent with the atomic map visualizations.

For the Cariaco Basin specimens, As, Ni, Cu, and Mn were detected in most specimens (Table 3). Areas of high trace element concentration were isolated to avoid mistaking them for clusters of inclusions. Manganese showed two distinct zones with low concentrations (L1, L2) and high concentrations (H1, H2). Based on the median μ value, the distribution of As was found to be mostly non-random (0.52). Nickel was mostly random, while Cu was mostly non-random (0.44 and 0.59, respectively). Manganese in the low concentration zones was found to be mostly non-random (0.56 and 0.67 for L1 and L2, respectively, in specimen 13379). In the high concentration zones, Mn was found to range from mostly random to predominantly non-random (0.27 and 0.88 in H1 and H2, respectively).

4. Discussion

4.1. LA-ICP-MS vs APT

4.1.1. Trace element composition of specimens

We compared the median bulk composition measured by APT with the trace element content measured during *in situ* analyses of entire framboids by LA-ICPMS (Large et al., 2014) with the goal of assessing trace element concentrations as determined using very different spatial resolutions. Two things to note are: (1) the number of samples differs significantly for LA-ICPMS vs. APT analyses (i.e., 14 framboids vs. 1 framboid for the Cariaco Basin, respectively) and (2) substructures rich in trace elements were targeted by APT, and therefore the concentrations of trace elements are expected to be higher than those for the analyses of the entire framboids (LA-ICPMS, Large et al., 2014).

Analyses via APT (this study) and LA-ICPMS (Large et al., 2014) from the modern Cariaco Basin are compared to emphasize the differences as a function of method used (reported as medians of all framboids analysed from the same sediment depth from which the APT framboids was taken). Overall, as expected, APT measures higher trace element concentrations compared to LA-ICP-MS: 540 ppm (APT) versus 202 ppm (LA-ICP-MS) for As, 2510 ppm versus 667 ppm for Ni, and 140 ppm versus 50.5 ppm for Co (Table 1). However, the APT Co concentration may be overestimated, as three tips were below detection limits and not included in the median. Copper is the only trace element with a lower concentration in the APT data relative the LA-ICP-MS results, with 385 ppm versus 747 ppm, respectively, although this may be because the highest concentration specimen measured by APT (1270 ppm Cu) is under represented by the median. The higher concentrations in the APT data in general may be due to overgrowths captured, which are thought to be more enriched in trace elements (Gregory et al., 2022a).

Table 2
Pearson coefficients of trace elements in Demerara Rise microtips.

Demerara Rise	Total ion cts	As	NiS_2	Cu	Mn
13367	9.00E+05		0.28	0.58	0.20
13369	9.00E+05				0.43
13370	2.00E+07	0.34		0.16	0.22
13676	4.40E+06	0.45	0.96	0.89	0.20
13679	3.80E+06			0.40	0.29
Median		0.40	0.62	0.49	0.22
Outliers				0.16	0.43

TEM imaging of pyrite framboids from Demerara Rise and the Cariaco Basin (Gregory et al.; 2022a) showed that Ni and Cu were highly concentrated in later pyrite, precipitated between the euhedral microcrystals that make up the bulk of the framboids. For both specimens, Ni is localized at microcrystal boundaries, in the later pyrite cement. Similarly, Cu is located predominantly in the pyrite overgrowth, while Mn had the highest concentration in the central, more euhedral pyrite grains.

The trace element trends observed by TEM (Gregory et al.; 2022a) were used to infer whether a grain boundary, a pyrite overgrowth, or a pyrite grain was captured in the APT specimens and to determine whether other trace elements were concentrated in these substructures. For Demerara Rise specimen #13676 (Fig. 3), later trace element-rich pyrite overgrowths are interpreted to be captured, as expressed by Ni localized within a linear feature, potentially reflecting the presence of a trace element rich microcrystal boundary. The zone of high Cu concentration overlaps with the Ni-rich zone but is thicker, extending further into the specimen, similar to what was observed in TEM data where the Cu-rich zone is thicker than the Ni zone (Gregory et al., 2022a). This overlap with the grain boundary suggests a possible relationship between Cu and Ni. Manganese is highly concentrated in the earliest, more euhedral pyrite generation. A lower Mn concentration is evident in the area where the proposed grain boundary and pyrite overgrowth resides. Atoms of As are evenly distributed throughout the specimen; hence, there is no zoning and no apparent relationship with other trace elements.

Among the Cariaco Basin specimens, #13379 (Fig. 4) is the clearest example of late trace element-rich pyrite overgrowths. The Ni-enriched zone L1 is interpreted to represent a secondary pyrite growth grain boundary as identified in the TEM data (Gregory et al., 2022a). At the grain boundary, As (Fig. 4) follows the same curve as Ni, suggesting a relationship between the two. This possibility is consistent with the interpretation that As substituted into the S site enhances the uptake of Ni (Deditius et al., 2008). The high concentration of Cu in this specimen also suggests that a pyrite overgrowth was captured. In addition to the zoning identified in the TEM images (Gregory et al., 2022a), we also identified zoning of Mn in the pyrite grain. These zones were isolated in IVAS to determine the relative atomic concentration of other trace elements (Fig. 5). Arsenic, Ni, and Cu have the highest concentrations in zone L1, suggesting that most trace elements are incorporated into areas with low Mn concentrations. Zone L2 is also a lower Mn concentration zone, where Ni records a spike in concentration.

4.2. Implications of trace elements incorporation in overgrowths

The identification of later pyrite trace element containing overgrowths in pyrite framboids suggests that significant trace element incorporation into pyrite occurs during diagenesis, even in euxinic settings where most of the pyrite is thought to have formed in the water column (e.g., Lyons, 1997). This observation suggests that pyrite trace element archives (Gregory et al., 2015; Large et al., 2014) are likely more analogous to bulk rock archives than direct measures of seawater trace element chemistry at the time of framboid formation. This relationship does not necessarily diminish the use of pyrite as a proxy of

Table 3
Pearson coefficients of trace elements in Cariaco Basin microtips.

Cariaco Basin	Total ion cts	AsS	NiS_2	Cu	Mn	Mn zones			
						L1	L2	H1	H2
13379	1.50E+06	0.53	0.69	0.69	0.14	0.56	0.67	0.27	0.88
13380	6.25E+05	0.50	0.48	0.47	0.27				
13384	5.00E+05	0.51	0.37	0.53	0.18				
13490	1.00E+06	0.67	0.40	0.65	0.21	0.56		0.30	
Median		0.52	0.44	0.59	0.20	0.56		0.28	
Outliers		0.67	0.69						

water chemistry because it still appears to capture the weakly held trace element reservoir. Further, the utility of pyrite methods is elevated because it can be preserved through metamorphism at higher grades compared to traditional bulk sample analyses. However, it needs to be understood that the analyses give a record of weakly held trace elements held by OM and Fe (hydr)oxides rather than direct seawater concentration. Further, detailed studies need to be conducted on pyrite formed in oxic settings where all pyrite is diagenetic to compare with the results of these euxinically deposited samples, where pyrite forms both in the water column and diagenetically in the sediments.

The observation that trace elements are incorporated into pyrite relatively late in some settings has implications for understanding the availability of trace elements for biologic processes. For example, Ni is an important co-factor in enzymes required for both anaerobic oxidation of methane and methanogenesis (Scheller et al., 2010). In this study, we can track the relative availability of Ni through diagenesis, with the Cariaco basin pyrite having relatively high Ni that is incorporated late, suggesting a high availability of Ni during later diagenesis (when methanogenesis is likely to have occurred) compared to the Demerara Rise sample, which had less Ni in its thicker late pyrite overgrowths. Similarly, Cu is an important enzymatic co-factor in the nitrogen cycle (for several reactions needed to convert NH_4^+ to NO_3^-) (Godfrey and Glass, 2011). In sediments where Cu is removed into pyrite rims during early diagenesis, nitrate production may be retarded in surface sediment layers and consequently so would biological activity. A similar argument has been made for the formation of pyrite nodules (Gregory et al., 2019); however, the resolution of trace element zoning, only achievable through APT analysis, shows that similar trapping of trace elements also occurs in fine-grained types of pyrite such as framboids. For this technique to be used to understand past metal availability during diagenesis, pyrite formation must be explored using analyses with the resolution capabilities presented here. Also, additional work on the pyrite proxy should seek to calibrate metal incorporation into pyrite in the context of known pore water trace element concentrations in modern sediments.

4.3. Trace element incorporation in framboidal pyrite

Framboidal textures in pyrite imply rapid growth, which enhances the incorporation of trace elements in large concentrations (e.g., Mn, Ni, Co, and Zn) (Raiswell and Plant, 1980; Butler and Rickard, 2000; Rickard, 2019); however, it is not known whether these trace elements are incorporated into nano-inclusions or occur as substitutions into the pyrite structure. NN analyses were used to determine whether any statistically significant clusters (i.e., nanoinclusions) are present, based on quantifying the degree of randomness of a trace element's atomic distribution (Fig. 6). Knowing how the trace elements are associated with the mineral phase is important because incorporation into the structure creates chemical and physical changes in the structure of the pyrite that can enhance or decrease the uptake of other trace elements, which can affect the partition co-efficient into pyrite. However, if an element is incorporated as nano-inclusions, they form their own mineral environment with a partition coefficient specific to the additional mineral species rather than pyrite.

Arsenic, Ni, Cu, and Mn were chosen for the nearest neighbor distribution analysis, as these were most consistently present in the samples from both sites. These trace elements were also concentrated in substructures with Ni concentrated at the grain boundary, Cu in the pyrite overgrowth, and Mn in the euhedral pyrite microcrystals. In the Demerara Rise APT specimen, the majority of the As and Mn was mostly random, suggesting it is usually held within the structure of the pyrite but occasionally forms small clusters. This is similar to Ni and Cu, which also showed mostly random distributions, although they did have occurrences where the distributions were non-random, consistent with visual observations of their elemental segregation to grain boundaries.

Arsenic, Ni, and Cu are held differently in the Cariaco Basin specimens compared to those from Demerara Rise, in that they are more likely to be non-randomly distributed. Notably, the trace element-rich pyrite rims around the pyrite microcrystals that make up the framboids are much thinner in the Cariaco Basin (Gregory et al., 2022a), and thus the higher amount of non-random elemental distributions may be due to the trace elements clustering along relatively thin planes rather than as nano-inclusions. The Mn distribution is more complicated in that Mn occurred as higher and lower concentration bands, although in both the high and low concentration cases the degree or randomness was mostly random, indicating that Mn is largely held within the pyrite structure. The presence of As corresponds to enrichments in Ni and Cu, suggesting there may be an enhancement in the uptake of these trace elements due to As substitution for S. This may be due to the Jahn-Teller effect (Radcliffe and McSween, 1969). In an octahedral ligand field, like a pyrite crystal, there are 9 d-electrons in Cu^{2+}. Thus, the Jahn-Teller effect causes the Cu^{2+} ions to distort the pyrite lattice, limiting pyrites ability to incorporate Cu (Radcliffe and McSween, 1969). However, if As substitutes for S one of the d-electrons from the Cu^{2+} ions is used in bonding with As. This removes the Jahn-Teller effect and stabilizes the pyrite lattice, allowing for more Cu to be incorporated (Radcliffe and McSween, 1969). The co-association of As with these trace elements indicates that As concentration should be taken into account both when developing experiments to better understand partition coefficients for pyrite trace element content and when interpreting how pyrite trace element content can inform the trace element content of the fluid in which the pyrite formed.

4.4. Comparison of data with expected trace element incorporation

The relative affinity of different trace elements for incorporation into pyrite have been suggested to be: As = Mo > Cu ≥ Co > Ni ≫ Mn > Zn > Cr = Pb > Cd (Morse and Luther, 1999). This relationship suggests that As and Cu and to a lesser extent Ni should be incorporated into pyrite relatively early, while Mn should be incorporated later. Further, it has been argued that Mn incorporation into pyrite may be prevented due to its fractionation and earlier incorporation into carbonate minerals. However, the data presented here seem to challenge these predictions, as Mn appears to be incorporated into early pyrite microcrystals, while As, Cu, and Ni are all concentrated later in the pyrite overgrowths that cement the earlier pyrite generations. This suggests that contrary to Morse and Luther, the rate of ligand exchange is dependant upon more than the rate of water removal from the inner hydration sphere. Thus, this observation suggests, more generally, that in natural, euxinic

settings, diagenetic reactions, such as de-sorption from organic matter or clays, are more important for the timing of trace element incorporation into pyrite than chemical properties of the individual elements being incorporated.

4.5. Limitations in quantification of APT data

While the APT technique has significant promise in trace element analyses of individual mineral phases, there are some limitations that should be noted. First, the technique should be viewed as semi-quantitative, as there are no existing standards for APT trace element analysis. This limitation will be difficult to overcome in the near term, as creating standard materials of pyrite that are homogenous in trace element content, at the nano-scale, as needed for APT, would be extremely difficult. Also, the errors reported in Table 1 reflect counting statistics of the instrument but do not take into account any possible peak overlaps or additional multi-element species that overlap with other, more abundant ions, that are not included in the data processing. However, even with these limitations, APT analysis provides an unparalleled 3D view of the position of atoms within pyrite at the nano-scale, and are thus a promising path to the mechanistic and timing details of elemental incorporation into pyrite—with important implications for the pyrite proxy.

5. Conclusions

In this study, we investigated As, Ni, Cu, Co, Mn, Sb, Se, and Ti in pyrite framboids from the Cariaco Basin and Demerara Rise. We found that most trace elements are held within trace element-rich regions that were interpreted to be later overgrowths of pyrite. This observation may be useful in understanding metal availability through diagenesis, with implications for understanding which biological processes were favored in ancient oceans. NN analyses showed that most elements are held predominantly within the pyrite structure, which suggests that partition coefficients for trace elements into pyrite may useful for understanding past fluid composition. However, due to the apparent two phases of trace element incorporation in pyrite framboids, even from euxinic settings, a direct link between pyrite chemistry and seawater chemistry is unlikely to be tenable unless the two pyrite phases can be accurately, quantitatively, measured. Further, previous predictions that As enhances the ability of pyrite to incorporate elements were supported, this suggests that As concentration should be taken into account when interpreting past fluid chemistry from pyrite chemistry.

Declaration of Competing Interest

The authors declare that they have no known competing financial interests or personal relationships that could have appeared to influence the work reported in this paper.

Acknowledgements

Sample preparation and LEAP 4000 XHR analyses were performed using Environmental and Molecular Sciences Laboratory, a national scientific user facility sponsored by the DOE Office of Biological and Environmental Research and located at PNNL. We further acknowledge funding through EMSL proposals 49860 to Lyons 50756 to Gregory, and the NSERC Discovery Grant funding to Gregory. J.D.O would like to acknowledge support from NASA Exobiology (80NSSC18K1532), and the National High Magnetic Field Laboratory (Tallahassee, Florida), supported by the National Science Foundation Cooperative Agreement No. DMR1644779 and the State of Florida. Funding was provided to T. W.L. through the NASA Astrobiology Institute under Cooperative Agreement No. NNA15BB03A issued through the Science Mission Directorate and the NASA Interdisciplinary Consortia for Astrobiology Research. We would also like the thank Steve Reddy, two anonymous reviewers and the associate editor, Brian Kendall, who's comments greatly improved the manuscript.

Appendix A. Supplementary material

The supplementary materials contain a brief explanation, with images, of the process involved in making the APT tips and details of the conditions used during APT analysis. Also, the appendices contain the raw data for the tip reconstructions. Supplementary material to this article can be found online at https://doi.org/10.1016/j.gca.2023.07.013.

References

Belousov, I., Large, R.R., Meffre, S., Danyushevsky, L.V., Steadman, J., Beardsmore, T., 2016. Pyrite compositions from VHMS and orogenic Au deposits in the Yilgarn Craton, Western Australia: Implications for gold and copper exploration. Ore Geol. Rev. 79, 474–499.

Brüske, A., Weyer, S., Zhao, M.-Y., Planavsky, N., Wegwerth, A., Neubert, N., Dellwig, O., Lau, K., Lyons, T., 2020. Correlated molybdenum and uranium isotope signatures in modern anoxic sediments: Implications for their use as paleo-redox proxy. Geochim. Cosmochim. Acta 270, 449–474.

Butler, I.B., Rickard, D., 2000. Framboidal pyrite formation via the oxidation of iron (II) monosulfide by hydrogen sulphide. Geochim. Cosmochim. Acta 64, 2665–2672.

Cassidy, K.F., Groves, D.I., McNaughton, N.J., 1998. Late-Archean granitoid-hosted lode-gold deposits, Yilgarn Craton, Western Australia: Deposit characteristics, crustal architecture and implications for ore genesis. Ore Geol. Rev. 13, 65–102.

Cook, N.J., Chryssoulis, S.L., 1990. Concentrations of invisible gold in the common sulfides. Can. Mineral. 28, 1–16.

Deditius, A.P., Utsunomiya, S., Renock, D., Ewing, R.C., Ramana, C.V., Becker, U., Kesler, S.E., 2008. A proposed new type of arsenian pyrite: Composition, nanostructure and geological significance. Geochim. Cosmochim. Acta 72, 2919–2933.

Dubosq, R., Gault, B., Hatzoglou, C., Schweinar, K., Vurpillot, F., Rogowitz, A., Rantitsch, G., Schneider, D.A., 2020. Analysis of nanoscale fluid inclusions in geomaterials by atom probe tomography: Experiments and numerical simulations. Ultramicroscopy 218.

Dubosq, R., Rogowitz, A., Schneider, D.A., Schweinar, K., Gault, B., 2021. Fluid inclusion induced hardening: nanoscale evidence from naturally deformed pyrite. Contrib. Mineral. Petrol. 176, 15.

Dubosq, R., Rogowitz, A., Schweinar, K., Gault, B., Schneider, D.A., 2019. A 2D and 3D nanostructural study of naturally deformed pyrite: assessing the links between trace element mobility and defect structures. Contrib. Mineral. Petrol. 174, 72.

Fleet, M.E., Mumin, A.H., 1997. Gold-bearing arsenian pyrite and marcasite and arsenopyrite from Carlin Trend gold deposits and laboratory synthesis. Am. Min. 82, 182–193.

Fougerouse, D., Reddy, S.M., Saxey, D.W., Rickard, W.D.A., van Riessen, A., Micklethwaite, S., 2016. Nanoscale gold clusters in arsenopyrite controlled by growth rate not concentration: Evidence from atom probe microscopy. Am. Min. 101, 1916–1919.

Fougerouse, D., Reddy, S.M., Kirkland, C.L., Saxey, D.W., Rickard, W.D., Hough, R.M., 2019. Time-resolved, defect-hosted, trace element mobility in deformed Witwatersrand pyrite. Geosci. Front. 10, 55–63.

Fougerouse, D., Reddy, S.M., Aylmore, M., Yang, L., Guagliardo, P., Saxey, D.W., Rickard, W.D., Timms, N., 2021. A new kind of invisible gold in pyrite hosted in deformation-related dislocations. Geology 49, 1225–1229.

Gault, B., Chiaramonti, A., Cojocaru-Mirédin, O., Stender, P., Dubosq, R., Freysoldt, C., Makineni, S.K., Li, T., Moody, M., Cairney, J.M., 2021. Atom probe tomography. Nat. Rev., Methods Primers 1, 51.

Godfrey, L.V., Glass, J.B., 2011. The geochemical record of the ancient nitrogen cycle, nitrogen isotopes, and metal cofactors. Meth. Enzymol. 486, 483–506.

Gopon, P., Douglas, J.O., Auger, M.A., Hansen, L., Wade, J., Cline, J.S., Robb, L.J., Moody, M.P., 2019. A nanoscale investigation of Carlin-type gold deposits: An atom-scale elemental and isotopic perspective. Econ. Geol. 114, 1123–1133.

Gopon, P., Douglas, J.O., Meisenkothen, F., Singh, J., London, A.J., Moody, M.P., 2022. Atom probe tomography for isotopic analysis: development of the 34S/32S system in sulfides. Microsc. and Microanalys. 28, 1127–1140.

Gregory, D.D., Large, R.R., Bath, A.B., Steadman, J.A., Wu, S., Danyushevsky, L., Bull, S. W., Holden, P., Ireland, T.R., 2016. Trace Element Content of Pyrite from the Kapai Slate, St. Ives Gold District, Western Australia. Econ. Geol. 111, 1297–1320.

Gregory, D.D., Large, R.R., Halpin, J.A., Baturina, E.L., Lyons, T.W., Wu, S., Danyushevsky, L., Sack, P.J., Chappaz, A., Maslennikov, V.V., Bull, S.W., 2015. Trace element content of sedimentary pyrite in black shales. Econ. Geol 110, 1389–1410.

Gregory, D.D., Lyons, T.W., Large, R.R., Jiang, G., Stepanov, A.S., Diamond, C.W., Figueroa, M.C., Olin, P., 2017. Whole rock and discrete pyrite geochemistry as complementary tracers of ancient ocean chemistry: An example from the Neoproterozoic Doushantuo Formation, China. Geochim. Cosmochim. Acta 216, 201–220.

Gregory, D.D., Kovarik, L., Taylor, S.D., Perea, D.E., Owens, J.D., Atienza, N.M., Lyons, T. W., 2022a. Nano-scale trace element zoning in pyrite framboids and implications for paleoproxy applications. Geology 50, 736–740.

Gregory, D.D., Lyons, T.W., Large, R.R., Stepanov, A., 2022b. Ground-truthing the pyrite trace element proxy in modern euxinic settings. Am. Min. 107, 848–859.
Gregory, D., Meffre, S., Large, R., 2014. Comparison of metal enrichment in pyrite framboids from a metal-enriched and metal-poor estuary. Am. Min. 99, 633–644.
Gregory, D., Mukherjee, I., Olson, S.L., Large, R.R., Danyushevsky, L.V., Stepanov, A.S., Avila, J.N., Cliff, J., Ireland, T.R., Raiswell, R., 2019. The formation mechanisms of sedimentary pyrite nodules determined by trace element and sulfur isotope microanalysis. Geochim. Cosmochim. Acta 259, 53–68.
Gueguen, B., Reinhard, C.T., Algeo, T.J., Peterson, L.C., Nielsen, S.G., Wang, X., Rowe, H., Planavsky, N.J., 2016. The chromium isotope composition of reducing and oxic marine sediments. Geochim. Cosmochim. Acta 184, 1–19.
Hughen, K.A., Overpeck, J.T., Peterson, L.C., Anderson, R.F., 1996a. The nature of varved sedimentation in the Cariaco Basin, Venezuela, and its palaeoclimatic significance. Geol. Soc. Spec. Publ. 116, 171–183.
Hughen, K.A., Overpeck, J.T., Peterson, L.C., Trumbore, S., 1996b. Rapid climate changes in the tropical Atlantic region during the last deglaciation. Nature 380, 51–54.
Hughen, K.A., Overpeck, J.T., Lehman, S.J., Kashgarian, M., Southon, J., Peterson, L.C., Alley, R.B., Sigman, D.M., 1998. Deglacial changes in ocean circulation from an extended radiocarbon calibration. Nature 391, 65–68.
Huston, D.L., Sie, S.H., Suter, G.F., Cooke, D.R., Both, R.A., 1995. Trace elements in sulfide minerals from eastern Australian volcanic-hosted massive sulfide deposits; Part I, Proton microprobe analyses of pyrite, chalcopyrite, and sphalerite, and Part II, Selenium levels in pyrite; comparison with delta 34 S values and implications for the source of sulfur in volcanogenic hydrothermal systems. Econ. Geol. 90, 1167–1196.
Large, R.R., Danyushevsky, L., Hollit, C., Maslennikov, V., Meffre, S., Gilbert, S., Bull, S., Scott, R., Emsbo, P., Thomas, H., Singh, B., Foster, J., 2009. Gold and trace element zonation in pyrite using a laser imaging technique: implications for the timing of gold in orogenic and carlin-style sediment-hosted deposits. Econ. Geol. 104, 635–668.
Large, R.R., Meffre, S., Burnett, R., Guy, B., Bull, S., Gilbert, S., Goemann, K., Danyushevsky, L., 2013. Evidence for an intrabasinal source and multiple concentration processes in the formation of the Carbon Leader Reef, Witwatersrand Supergroup, South Africa. Econ. Geol. 108, 1215–1241.
Large, R.R., Halpin, J.A., Danyushevsky, L.V., Maslennikov, V.V., Stuart, W., Bull, L.J.A., Gregory, D.D., Lounejeva, E., Lyons, T.W., Sack, P.J., McGoldrick, P.J., Calver, C.R., 2014. Trace element content of sedimentary pyrite as a new proxy for deep-time ocean–atmosphere evolution. EPSL 389, 209–220.
Larson, D.J., Prosa, T.J., Ulfig, R.M., Geiser, B.P., Kelly, T.F., 2013a. Specimen Preparation. In: Larson, D.J., Prosa, T.J., Ulfig, R.M., Geiser, B.P., Kelly, T.F. (Eds.), LocAl Electrode Atom Probe TomogrAphy: A User's Guide. Springer, New York, New York, NY, pp. 25–53.
Larson, D.J., Prosa, T.J., Ulfig, R.M., Geiser, B.P., Kelly, T.F., 2013b. Local Electrode Atom Probe Tomography. Springer, New York, New York, NY.
Leckie, R.M., Sigurdsson, H., Acton, G.D., Draper, G. (Eds.), 2000. Proceedings of the Ocean Drilling Program, 165 Scientific Results. Ocean Drilling Program.
Lowers, H.A., Breit, G.N., Foster, A.L., Whitney, J., Yount, J., Uddin, M.N., Muneem, A. A., 2007. Arsenic incorporation into authigenic pyrite, Bengal Basin sediment, Bangladesh. Geochim. Cosmochim. Acta 71, 2699–2717.
Lyons, T.W., 1997. Sulfur isotopic trends and pathways of iron sulfide formation in upper Holocene sediments of the anoxic Black Sea. Geochim. Cosmochim. Acta 61, 3367–3382.
Lyons, T.W., Werne, J.P., Hollander, D.J., Murray, R.W., 2003. Contrasting sulfur geochemistry and Fe/Al and Mo/Al ratios across the last oxic-to-anoxic transition in the Cariaco Basin, Venezuela. Chem. Geol. 195, 131–157.
Meffre, S., Large, R.R., Scott, R., Woodhead, J., Chang, Z., Gilbert, S.E., Danyushevsky, L. V., Maslennikov, V., Hergt, J.M., 2008. Age and pyrite Pb-isotopic composition of the giant Sukhoi Log sediment-hosted gold deposit, Russia. Geochim. Cosmochim. Acta 72, 2377–2391.
Michel, D., Giuliani, G., Olivo, G.R., Marini, O.J., 1994. As growth banding and the presence of Au in pyrites from the Santa Rita gold vein deposit hosted in Proterozoic metasediments, Goias State, Brazil. Econ. Geol. 89, 193–200.
Miller, M.K., Forbes, R.G., 2009. Atom probe tomography. Mater. Charact. 60, 461–469.
Miller, M.K., Forbes, R.G., 2014. Atom-Probe Tomography: The Local Electrode Atom Probe. Springer, US.
Morse, J., Luther, G., 1999. Chemical influences on trace metal-sulfide interactions in anoxic sediments. Geochim. Cosmochim. Acta 63, 3373–3378.
Mosher, D.C., Erbacher, J., Malone, M.J. (Eds.), 2007. Proceedings of the Ocean Drilling Program, 207 Scientific Results. Ocean Drilling Program.
Perea, D.E., Arslan, I., Liu, J., Ristanović, Z., Kovarik, L., Arey, B.W., Lercher, J.A., Bare, S.R., Weckhuysen, B.M., 2015. Determining the location and nearest neighbours of aluminium in zeolites with atom probe tomography. Nat. Com. 6, 7589.
Piper, D.Z., Dean, W.E., 2002. Trace-element deposition in the Cariaco Basin, Venezuela Shelf, under sulfate-reducing conditions: A history of the local hydrography and global climate, 20 ka to the present. US Geolog. Survey 2330–7102.
Qian, G., Brugger, J., Testemale, D., Skinner, W., Pring, A., 2013. Formation of As (II)-pyrite during experimental replacement of magnetite under hydrothermal conditions. Geochim. Cosmochim. Acta 100, 1–10.
Radcliffe, D., McSween, H.Y., 1969. Copper zoning in pyrite from Cerro de Pasco, Peru: a discussion. Am Min. J. Earth Planet. Mater. 54, 1216–1217.
Raiswell, R., Plant, J., 1980. The incorporation of trace elements into pyrite during diagenesis of black shales, Yorkshire, England. Econ. Geol. 75, 684–699.
Raven, M.R., Fike, D.A., Bradley, A.S., Gomes, M.L., Owens, J.D., Webb, S.A., 2019. Paired organic matter and pyrite δ34S records reveal mechanisms of carbon, sulfur, and iron cycle disruption during Ocean Anoxic Event 2. EPSL 512, 27–38.
Reddy, S.M., Saxey, D.W., Rickard, W.D.A., Fougerouse, D., Montalvo, S.D., Verberne, R., van Riessen, A., 2020. Atom probe tomography: development and application to the geosciences. Geostand. Geoanal. Res. 44, 5–50.
Reich, M., Becker, U., 2006. First-principles calculations of the thermodynamic mixing properties of arsenic incorporation into pyrite and marcasite. Chem. Geol. 225, 278–290.
Reich, M., Kesler, S.E., Utsunomiya, S., Palenik, C.S., Chryssoulis, S.L., Ewing, R.C., 2005. Solubility of gold in arsenian pyrite. Geochim. Cosmochim. Acta 69, 2781–2796.
Rickard, D., 2012. Sulfidic sediments and sedimentary rocks. Newnes.
Rickard, D., 2019. How long does it take a pyrite framboid to form? EPSL 513, 64–68.
Rickard, D., 2021. Framboids. Oxford University Press, p. 334.
Scheller, S., Goenrich, M., Boecher, R., Thauer, R.K., Jaun, B., 2010. The key nickel enzyme of methanogenesis catalyses the anaerobic oxidation of methane. Nature 465, 606–608.
Stephenson, L.T., Moody, M.P., Liddicoat, P.V., Ringer, S.P., 2007. New techniques for the analysis of fine-scaled clustering phenomena within atom probe tomography (APT) data. Microsc. Microanaly. 13, 448–463.
Taylor, S.D., Liu, J., Arey, B.W., Schreiber, D.K., Perea, D.E., Rosso, K.M., 2018. Resolving Iron(II) Sorption and Oxidative Growth on Hematite (001) Using Atom Probe Tomography. J. Phys. Chem. 122, 3903–3914.
Taylor, S.D., Liu, J., Zhang, X., Arey, B.W., Kovarik, L., Schreiber, D.K., Perea, D.E., Rosso, K.M., 2019. Visualizing the iron atom exchange front in the Fe(II)-catalyzed recrystallization of goethite by atom probe tomography. PNAS 116, 2866–2874.
Taylor, S.D., Gregory, D.D., Perea, D.E., Lyons, T.W., 2022. Resolving paleoseawater signatures in nanoscale fluid inclusions by atom probe tomography. EPSL 599, 117859.
Thompson, K., Lawrence, D., Larson, D.J., Olson, J.D., Kelly, T.F., Gorman, B., 2007. In situ site-specific specimen preparation for atom probe tomography. Ultramicroscopy 107, 131–139.
Thunell, R.C., Sigman, D.M., Muller-Karger, F., Astor, Y., Varela, R., 2004. Nitrogen isotope dynamics of the Cariaco Basin, Venezuela. Glob. Biogeochem. Cycles 18.
Tribovillard, N., Algeo, T.J., Lyons, T., Riboulleau, A., 2006. Trace metals as paleoredox and paleoproductivity proxies: an update. Chem. Geol. 232, 12–32.
Wang, Q., Morse, J.W., 1996. Pyrite formation under conditions approximating those in anoxic sediments I. Pathway and morphology. Mar. Chem. 52, 99–121.
Wilkin, R.T., Barnes, H.L., 1997. Formation processes of framboidal pyrite. Geochim. Cosmochim. Acta 61, 323–339.
Wu, Y.F., Fougerouse, D., Evans, K., Reddy, S.M., Saxey, D.W., Guagliardo, P., Li, J.-W., 2019. Gold, arsenic, and copper zoning in pyrite: A record of fluid chemistry and growth kinetics. Geology 47, 641–644.